Solid State Ionics 298 (2016) 1–8

Contents lists available at ScienceDirect

Solid State Ionics

journal homepage: www.elsevier.com/locate/ssi

Model composite microelectrodes as a pathfinder for fully oxidic SOFC anodes

Matthias Gerstl [a,b,*], Alexander Hutterer [a], Jürgen Fleig [a], Martin Bram [b,c], Alexander Karl Opitz [a,b]

[a] Institute of Chemical Technologies and Analytics, TU Wien, Getreidemarkt 9/164-EC, A-1060 Vienna, Austria
[b] Christian Doppler Laboratory for Interfaces in Metal-Supported Electrochemical Energy Converters, Forschungszentrum Jülich, D-52425 Jülich, Germany
[c] Institute of Energy Research (IEK-1), Forschungszentrum Jülich, D-52425 Jülich, Germany

ARTICLE INFO

Article history:
Received 9 August 2016
Received in revised form 7 October 2016
Accepted 21 October 2016
Available online 2 November 2016

Keywords:
Model composite
All-oxide anode
Micro-patterned anode
Sulphur tolerance
Impedance spectroscopy
AZO
GDC
STO
Electronic conductivity

ABSTRACT

All-oxide model-composite electrodes were established consisting of a thin, micropatterned, electronically conducting oxide, which acts as a current collector, and a thin film of gadolinia-doped ceria, which is an electrochemically highly active mixed conductor under reducing atmospheres. The choice of the current collecting oxides was based on their electronic conductivity assessed by measurements of thin films using the van der Pauw method. Lanthanum and niobium doped strontium titanate as well as alumina doped zinc oxide, were investigated this way in a humid hydrogen atmosphere. Promising materials were incorporated as a current collector into model-composite microelectrodes and tested for their stability and efficiency in electrochemically activating the microelectrode. Alumina doped zinc oxide, while being an excellent electron conductor, showed severe stability problems at temperatures above 600 °C. However, a microelectrode with a current collector of niobium doped strontium titanate ($Sr_{0.9}Ti_{0.8}Nb_{0.2}O_3$) performed comparable to an electrode with a Pt current collector and, additionally, showed an improved tolerance to sulphur poisoning in a humid hydrogen atmosphere with 10 ppm of hydrogen sulphide.

1. Introduction

Traditionally, the anode of a solid oxide fuel cell (SOFC) consists of a cermet structure, made up of a percolating network of a metallic nickel phase and yttria stabilized zirconia (YSZ). The nickel serves as a catalyst for the fuel gas oxidation and provides electronic conduction, while the oxide ions are transported via the YSZ to the electrochemically active triple phase boundary (TPB) [1]. This setup is well researched and performs admirably in the application case. However, an inherent drawback of using a metallic current collector is its limited redox stability, restricting its application envelope to reducing atmospheres [2]. Therefore, protective measures, like applying a cathodic bias, have to be taken to avoid oxidation during stand times [3].

Another issue with Ni/YSZ cermet anodes is their low tolerance for sulphur containing gases like diesel reformate, natural gas or methane from biogenic sources, which are important prospective fuels. Concentrations of a few ppm hydrogen sulphide in the feed gas are enough to cause irreversible degradation, which is commonly referred to as sulphur poisoning [4–6].

Both problems may be tackled by substituting nickel and YSZ with different (particularly oxidic) materials [7–9]. Alumina doped zinc oxide (AZO) and donor doped strontium titanate (STO) exhibit good electronic conductivity and may be an alternative to nickel in terms of current collection. On the other hand, gadolinia doped cerium oxide (GDC) not only is a good oxygen ion conductor, but also shows electronic conductivity in reducing atmospheres, which would allow an enlarged reactive surface area compared to the TPB-active Ni/YSZ [10]. Additionally, GDC offers good catalytic activity towards hydrogen oxidation [10,11], which is of high importance especially in a nickel-free anode. Finally, both doped STO [5,12,13] and GDC [4–6,14] have been discussed in literature for their higher sulphur poisoning tolerance than Ni/YSZ based anodes.

In this study, thin films of the electron conducting oxides AZO, La-doped STO, and Nb-doped STO were prepared and electrically characterized in reducing atmospheres using the van der Pauw method [15]. The most promising materials in terms of electronic conductivity were integrated as current collectors in model-composite microelectrodes together with gadolinia doped ceria as the electrochemically active phase. Results of first experiments regarding the electrochemical performance as well as the sulphur tolerance are presented for fully oxidic model-composite microelectrodes with Nb-doped STO current collectors.

* Corresponding author at: Institute of Chemical Technologies and Analytics, TU Wien, Getreidemarkt 9/164-EC, A-1060 Vienna, Austria.
E-mail address: matthias.gerstl@tuwien.ac.at (M. Gerstl).

http://dx.doi.org/10.1016/j.ssi.2016.10.013

2. Experimental

The PLD target for the AZO thin films was prepared by a mixed oxide route using ZnO and 2 wt% Al_2O_3 powder, both purchased from Sigma Aldrich, USA. PLD-targets for the layers of GDC-20 were prepared from 20 mol% Gd_2O_3 doped CeO_2 (Treibacher, Austria). The PLD targets for the doped STO titanate thin films were also prepared by the mixed oxide route, using La_2O_3, Nb_2O_5 and $SrCO_3$ all purchased from Sigma Aldrich, USA in purities better than 99.99%. A KrF excimer laser (Coherent Lambda Physics, Germany) operating at $\lambda = 248$ nm with a pulse length of 50 ns was used to ablate the targets. The distance between target and substrate was fixed at 6 cm. The parameters for the ablation process are listed in Table 1.

For van der Pauw measurements AZO layers were prepared on 9.5 mol% yttria stabilized zirconia (YSZ), while doped STO layers were prepared on magnesia. Both substrates were polished 1×1 cm^2 (100) single crystals with a thickness of 0.5 mm purchased from Crystec, Germany. In-plane resistivity measurements of the thin films were also performed in a quartz tube. Four platinum needles were placed on top of the thin film in the corners of a 10×10 mm^2 sample as close as possible to the sample boundary to meet the prerequisites of the van der Pauw method [15]. In case of the AZO layers additional 200 nm thick Pt layers were deposited on the corners by magnetron sputtering (MED-020 coating system, Bal—Tec, Germany) to improve the contact quality. The quartz apparatus was uniformly heated in a tube furnace and temperature was measured by means of an encapsulated type K thermoelement positioned adjacent to the sample. A precision voltage source (Keithley 2410) and a multimeter (Keithley 2000) were used during the course of the measurements.

Premixed gases of ca. 2.5% H_2 in Ar (ARCAL 10) and 200 ppm H_2S in ARCAL 10 were purchased from Air Liquide (Germany) in purities better than 99.99%. Dilution of the concentrated hydrogen sulphide carrying gas was realized by analog mass flow controllers. The H_2S free ARCAL 10 was bubbled through deionized water at room temperature to achieve a water to hydrogen ratio of about 1:1.

For preparation of model-composite electrodes current collectors consisting of 100 nm thin Pt films on a 5 nm thick Ti adhesion layer were both deposited by magnetron sputtering, while AZO, STO and GDC layers were prepared by pulsed laser deposition (PLD), for the employed parameters see Table 1. Micro-patterning of the current collectors and the GDC layers was done using photolithography with subsequent Ar ion beam etching in a vacuum chamber. Details on the size and shape of the obtained microelectrodes are shown in the results section. Counter electrodes were prepared by applying Pt paste (Gwent Electronic Materials, UK) on the back side of YSZ single crystals.

EDX spectra were recorded on a Quanta 200 scanning electron microcsope (FEI, The Netherlands).

Impedance spectra were recorded using an Alpha-A high-performance frequency analyzer (Novocontrol, Germany) in the frequency range of 1 MHz to 50 mHz with an ac signal of 10 mV root-mean-square. Impedance measurements were performed in a micro-contact setup on a heating stage (Linkam, UK), which allowed variable gas atmospheres, except the sulphur poisoning experiments on model-composite electrodes, which were done in a symmetrically heated three-terminal micro-contact setup. Both setups are described in detail in Ref. [16].

Table 1
Parameters for the pulsed laser deposition (PLD) process of the preparation of AZO, doped STO (LST-19, LST-46, STN 982) and GDC-20 thin films. Distance between target and substrate was fixed at 6 cm, the temperature was controlled by a pyrometer.

Target material	Laser energy [mJ]	Laser pulse rate [Hz]	Substrate temperature [°C]	pO_2 [mbar]
AZO	250	10	25	2×10^{-2}
Doped STO/GDC-20	400	5	650	4×10^{-2}

3. Results and discussion

3.1. Choice of oxidic current collectors

AZO could not be grown on insulating substrates with sufficent quality, but good growth results could be achieved on YSZ single crystals. The electronic conductivity of AZO thin films on YSZ in reducing atmosphere was measured by the van der Pauw method. Ionic current contributions from the substrate can safely be neglected, since at lower temperatures the ionic conductivity of YSZ proved to be more than five orders of magnitude smaller than the electronic conductivity of AZO. In Fig. 1 the conductivities of two 500 nm thick layers of AZO are plotted, each measured in a different temperature range. Up to a maximum temperature of about 620 °C, see squares in Fig. 1, the conductivity is fairly constant between the heating (closed squares ■) and cooling part (open squares □) of the cycle. Furthermore, the absolute values of the conductivity in excess of 1000 S/cm are very high for an oxide, though in a typical range of AZO thin films [17,18]. However, starting at about 650 °C the AZO layer shows an irrversible conductivity degradation by about two orders of magnitude to less than 20 S/cm. True values might be even lower since here ionic contributions from current in the YSZ substrate cannot be excluded. This conductivity drop is most likely linked to zinc or zinc oxide evaporation, as evidenced by the EDX spectra shown later in section 3.2.1 (Fig. 6b). As 650 °C is already on the lower end of typical fuel cell operating temperatures of about 600 °C to 1000 °C [19], AZO may only (if at all) be a prospective alternative current collector material for intermediate temperature SOFCs.

In Fig. 2 the conductivities of differently donor doped strontium titanate thin films on magnesia substrates are plotted versus temperature. The compositons, chosen from literature [20] due to their high reported conductivies and easy availability of the raw materials, were: $Sr_{0.9}Ti_{0.8}Nb_{0.2}O_3$ (STN-982) [21], $La_{0.4}Sr_{0.6}TiO_3$ (LST-46) [22] and $La_{0.1}Sr_{0.9}TiO_3$ (LST-19) [23]. As expected, the higher donor concentration in LST-46 causes a significantly higher electrical conductivity compared to LST-19. However, after heating to about 950 °C, the high conductivities of LST-46 are not reproduced in the measurements taken while cooling down. Besides the donor concentration, the electrical conductivity of donor doped strontium titanates also very much depends on the history of the sample, namely which oxygen partial pressure it was exposed to at which temperatures [24]. All samples were measured in a dry hydrogen atmosphere before the data was recorded in a humidified reducing atmosphere, plotted in Fig. 2. Therefore, it is likely that the high conductivities of LST-46 during heating of

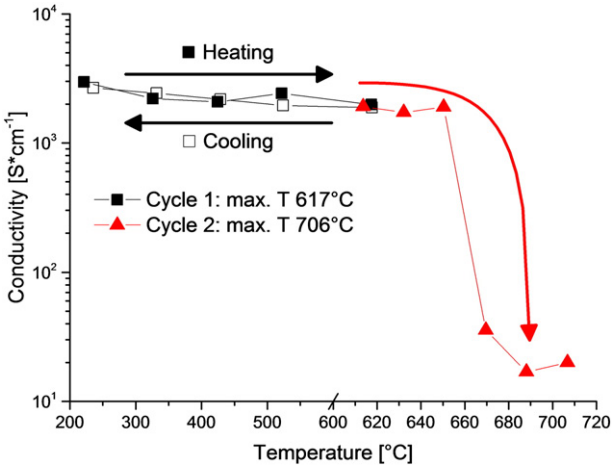

Fig. 1. Total conductivity measurements of two 500 nm thick AZO layers with 2 wt% alumina doping deposited on YSZ single crystals using the van der Pauw method. Measurements were performed in humidified ~2.5 vol% H_2 in Ar, with a ratio of hydrogen to water of 1:1.

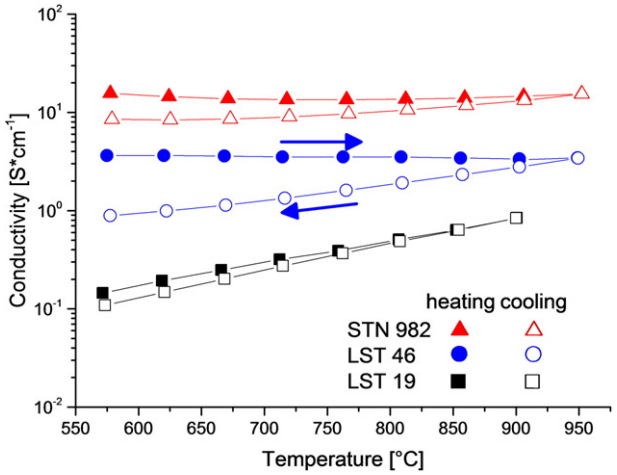

Fig. 2. Total conductivity measurements of 200 nm thick layers of n-doped strontium titanate on magnesia single crystals using the van der Pauw method. Measurements were performed in humidified ~2.5 vol% H_2 in Ar, with a ratio of hydrogen to water of 1:1. Abbreviations: STN-982 … $Sr_{0.9}Ti_{0.8}Nb_{0.2}O_3$; LST-46 … $La_{0.4}Sr_{0.6}TiO_3$; LST-19 … $La_{0.1}Sr_{0.9}TiO_3$.

the sample were in fact caused by retention of the higher conductivity during the more reducing conditions of the pre-treatment.

The Nb doped STN-982 layer exhibits the highest conductivity of the materials probed in this study in a temperature range relevant for SOFCs of roughly 750 to 900 °C and was consequently chosen for further investigations. In Fig. 3 additional conductivity measurements, labelled cycle 2 to 11, are compared to the data shown in Fig. 2, labelled cycle 1. The second cycle is an exact repetition of cycle 1 with measurements first in a dry and subsequently humidified hydrogen atmosphere. As with LST-46, the conductivities recorded during heating the sample are significantly higher than during the cool down part of the temperature cycles 1 and 2. As before, the cause is most likely a retention of a higher conductive state due to the previous reduction and a resulting higher electron concentration [24]. However, already a lower conductivity of an order of magnitude is observed in the second cycle compared to the first one, as well as a change in the temperature dependence despite nominally identical pre-history. This already indicates a very high

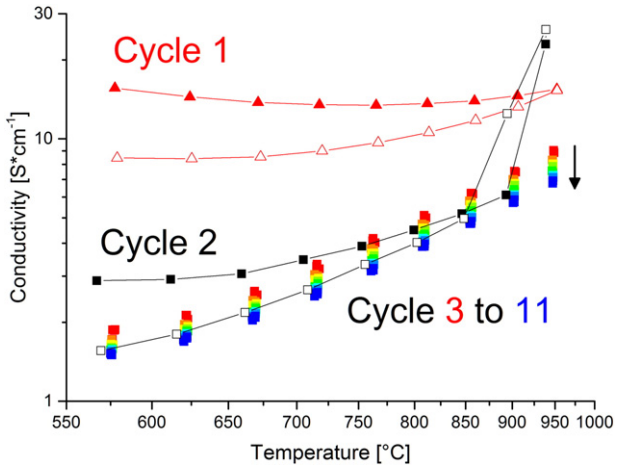

Fig. 3. Multiple total conductivity measurements of a 200 nm thick layer of $Sr_{0.9}Ti_{0.8}Nb_{0.2}O_3$ on a magnesia single crystal using the van der Pauw method. Measurements were performed in humidified ~2.5 vol% H_2 in Ar, with a ratio of hydrogen to water of 1:1. Previous to the measurements of cycle 1 and 2 the sample was measured in a dry hydrogen atmosphere. Cycles 3 to 11 were recorded consecutively without previous reduction in dry hydrogen, the arrow indicates a successive decline in the conductivity.

sensitivity of the materials towards its pretreatment. Additional conductivity data were recorded in temperature cycles 3 to 11 in a humid hydrogen atmosphere to exclude any non-equilibrium conductivity due to a previous reduction. The data agree very well with the cool down part of cycle 2, hence, it can be concluded that the sample is now fully equilibrated. However, a slower degradation of the conductivity, indicated by an arrow in Fig. 3, is observed. A very recent theoretical study proposed a transition of Nb doped STO from electronic to vacancy compensation upon oxidation by diffusion of Sr vacancies into the STO bulk [25]. While this model was calculated for 1500 K, some studies suggest that the relevant processes may also be significant below 1100 K [26–28] and might offer an explanation for the slow degradation encountered in the present work. Nevertheless, even after these conductivity decreases, STN-982 still remains the material with the highest conductivity of the investigated titanate based materials.

3.2. Feasibility of oxidic current collectors in microelectrode experiments

For a meaningful interpretation of electrochemical measurements on thin film microelectrodes, a homogeneous polarization of the complete electrode has to be guaranteed. Cerium oxide is a moderate electronic conductor in reducing conditions [29], but its electronic conductivity is insufficient to polarize a 200 nm thin film microelectrode of more than a few tens of microns in size [10,30]. Therefore, an additional current collector phase is needed. The current collectors used in this study all have a spacing smaller than 15 μm, which has been shown to be more than sufficient [10]. In Fig. 4 the three different model composite electrode types prepared on YSZ single crystals are shown schematically: Electrode type A has a Pt current collector buried beneath a GDC-20 thin film, shown in Fig. 4a); type B is prepared with an oxidic current collector on top of the electrode, see Fig. 4b); while type C has a buried Pt current collector as well as an oxidic one on top, as plotted in Fig. 4c). The contacting setup is sketched in Fig. 4d).

3.2.1. AZO

Model composite microelectrodes of type B (see Fig. 4b), using AZO with 2 wt% alumina doping as a current collector were prepared and measured at 550 °C in a humid hydrogen atmosphere. In the inset of Fig. 5 the exact shape of the current collector in the 395 × 160 μm^2 sized microelectrode is shown. Six impedance spectra taken in short intervals on the same electrode are plotted in Fig. 5. Even within this short time of roughly 20 min, a severe change of the shape of the low frequency semi-circle from fairly ideal to strongly depressed is observed. A Kramers-Kronig analysis (details not shown) revealed severe non steady state behaviour in the impedance data [31,32]. Therefore, no reliable fitting of the data is possible. In the corresponding optical micrographs in the insets in Fig. 5 a pronounced colour change is visible in the AZO current collector. Interestingly, the pristine electrodes next to the measured one show no such alterations, confer Fig. 6a). Comparing the EDX spectra of a neighbouring electrode with the degraded measured one (Fig. 6b)), a severe depletion of Zn is found, which can account for the degradation phenomena. Furthermore, the degradation found in the van der Pauw experiments, see Fig. 1, is most likely caused by a similar mechanism. It seems that AZO under the measurement conditions is very close to its stability limit and the slight polarization either due to thermo-electric effects of the asymmetrically heated setup [16] in combination with the cooling effect of the Pt contacting tip or the AC signal of the impedance spectrometer is enough to cause a fast degradation. Either way, again it can be concluded that AZO is not well-suited as a potential alternative oxidic current collector for SOFC anodes. Moreover, due to the high reactivity of hydrogen sulphide with zinc oxide, which is in fact used as a desulphurizing agent in hydrocarbon purification [33], no sulphur tolerance measurements were performed using AZO current collectors.

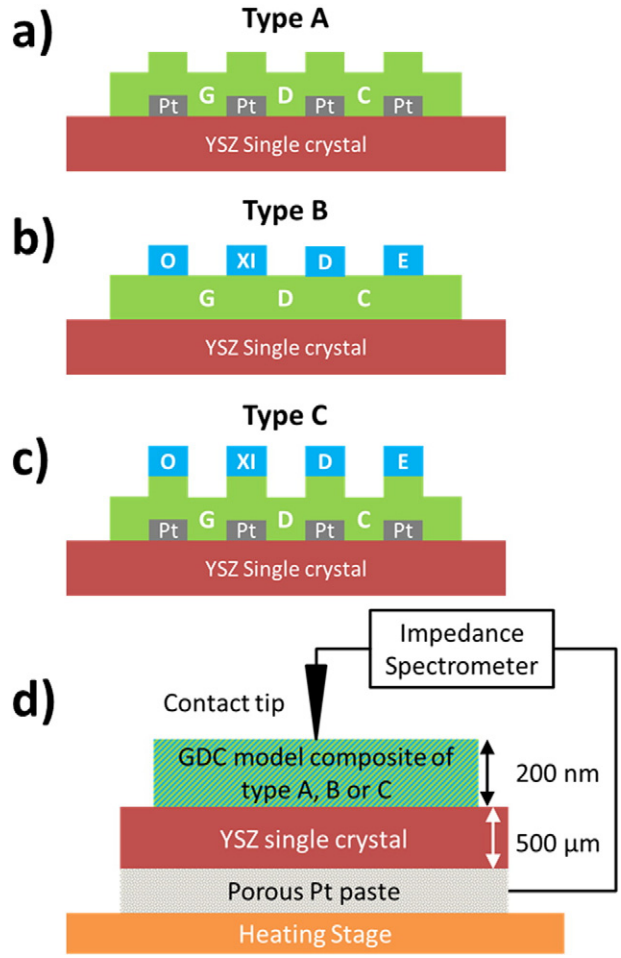

Fig. 4. Types of model-composite microelectrodes used. a) Type A: 100 nm thick Pt current collector on a 5 nm Ti adhesion layer buried under 200 nm thick GDC-20 thin film. b) Type B: 200 nm GDC-20 thin film with oxide current collector on top. The latter was either 100 nm AZO, or 200 nm STN-982. c) Type C: Combination of type A and B, buried Pt current collector beneath a GDC layer and oxide current collector on top, only STN-982 was used in this configuration. d) Measurement setup of the microelectrode measurements.

3.2.2. STN-982

AZO showed an extraordinary high electronic conductivity in its stability regime, see Fig. 1, while STN-982 is a significantly worse conductor; compare Fig. 2 and Fig. 3. Nb doped STO is being considered by several studies as a potential candidate for an oxide current collector [34,35] and tests have been performed with porous composites [36,37]. While some authors concede that the long term stability needs additional studies, conductivities are generally presumed to be sufficient [37]. Therefore, it is necessary to verify whether or not an STN-982 current collector is able to transport charge also to the edges of the contacted microelectrodes. The strategy to assess this is explained in the following section.

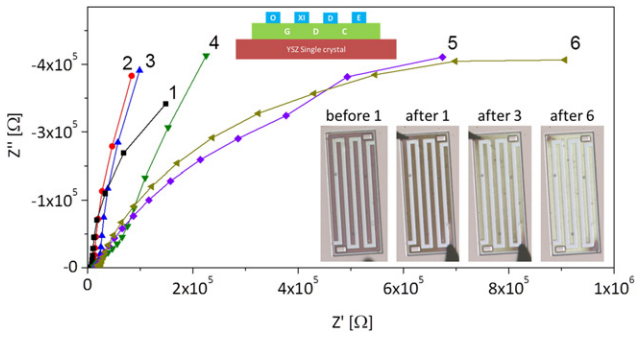

Fig. 5. Nyquist plots of electrochemical impedance spectra taken on a 395 × 160 µm² electrode of type B, see Fig. 4b), with a 100 nm AZO current collector on a 200 nm GDC-20 thin film. The width of the current collector fingers was 15 µm with a spacing of 11.7 µm. The degradation between spectrum 1 and 6 happened in a 20 min time span. The optical micrographs in the inset highlight the colour change of the AZO current collector from dark to bright during the measurements. Measurements were performed at 550 °C in an asymmetrically heated setup in a gas atmosphere of humidified ~2.5 vol% H_2 in Ar, with a ratio of hydrogen to water of 1:1.

In Fig. 7a) a schematic top view of a GDC model composite microelectrode with a grid-shaped current collector is plotted, which has been contacted in the centre by a metal tip, cf. Fig. 4d) for a side-view sketch of the same setup. One strip of the current collector in Fig. 7) is magnified in Fig. 7b) and c) to highlight the charge transport, the perpendicular strips have been neglected for clarity. If the current collector exhibits sufficient electronic conductivity or the diameter of the electrode is small enough, the charge is transported across the entire microelectrode and the complete GDC surface is active for the electrochemical surface reaction. This case is sketched in Fig. 7b). However, should the electronic conductivity of the current collector be insufficient or the diameter of the microelectrode too large, then the electronic charge carriers will not reach the edges of the probed microelectrode and only a fraction of the GDC surface will be electrochemically active. This case is plotted in Fig. 7c). Both cases are described with the transmission-line type equivalent circuit plotted in Fig. 7d): The electronic charge carriers travel along the upper rail representing the current collector (blue region) and are converted into oxygen ions via the surface reaction (green region). The oxygen incorporation reaction – in its simplest approximation – can be described by a parallel connection of the polarization resistance and the chemical capacitance of the GDC layer [38–40]. It should be noted that the ionic transport in GDC above or below the current collector, causes a feature in the medium frequency range of the impedance spectrum [38]. However, since the surface resistance is well separated, this effect is not relevant for our consideration and can safely be neglected in the equivalent circuit in Fig. 7d). Once incorporated, the oxygen ions are transported to the counter electrode through the YSZ bulk (red region).

Please note that the impedance of the counter electrode is neglected in the circuit in Fig. 7d), which can reasonably be assumed due to the size difference of at least 3 orders of magnitude compared to the microelectrode [41].

Typical impedance spectra measured on a 300 µm diameter composite microelectrode of type C, which are taken at different time intervals, are shown in Fig. 8; the shape of the current collector becomes visible in the micrograph inset. Given a good conductivity in the current collector, the electronic rail can be considered as short-circuited and the rather complex equivalent circuit in Fig. 7d) is simplified to the one shown in Fig. 8. This circuit consists of a high frequency resistance R_{HF}, which includes the total ionic resistance of the YSZ bulk (and the impedance caused by ion transport in GDC either above or below the current collectors, see above) in series with the total surface polarization resistance R_{surf} in parallel to the chemical capacitance of the whole GDC layer C_{chem}. Only the low frequency parts from about 1 Hz to 50 mHz were used for fitting, which did not vary for the different electrode types. This part has been shown in previous work to almost exclusively consist of the parallel connection of the surface polarization resistance R_{surf} with the chemical capacitance C_{chem} [38–40].

In principle, the numerical value of the three elements R_{surf}, C_{chem} and the bulk YSZ resistance is a function of the probed area: The YSZ bulk and surface resistance should scale inversely with the active microelectrode area. Keeping the thickness of electrodes constant the chemical capacitance is directly related to the electrodes area. Therefore, one should be able to judge the sufficiency of the electronic conductivity in the current collector by varying the microelectrode diameter and check if the expected trends or deviations from a linear correlation are observed.

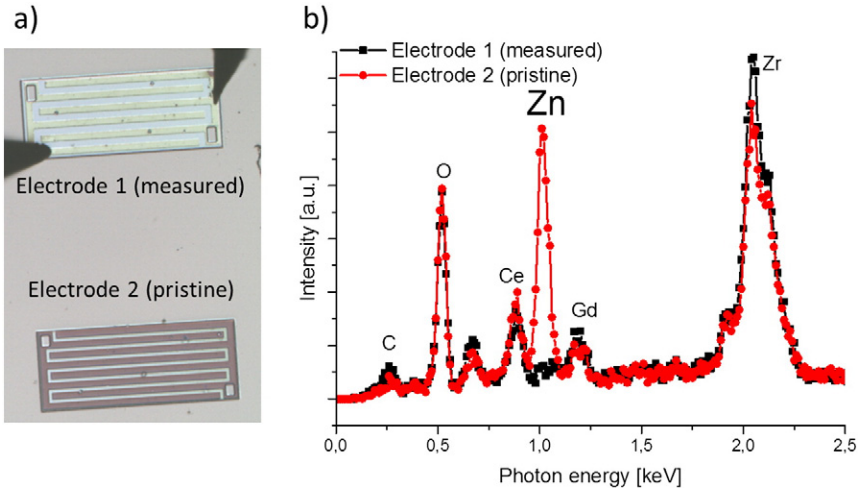

Fig. 6. a) Optical micrograph of 395 × 160 μm^2 electrodes of type B, see Fig. 4b), with a 100 nm AZO current collector on top of 200 nm GDC-20. The width of the current collector fingers was 15 μm with a spacing of 11.7 μm. The measured electrode 1 is the same as in Fig. 5, the neighbouring electrode is pristine, but was exposed to the same temperature and atmosphere. b) EDX spectra of the electrodes shown in a); note the depletion of Zn in the measured electrode.

However, due to practical reasons, only the chemical capacitance of the GDC layer is considered a valid measure, which should be briefly argued in the following. The asymmetric heating stage used causes the contacted microelectrodes to be at a considerably lower temperature due to the cooling effect of the needle, an effect that is especially pronounced for electrodes of diameters below 50 μm [16]. The YSZ bulk conductivity [42] and the GDC polarization resistance [43] are thermally activated processes; hence, both are unfit for comparison of different microelectrode sizes. Moreover, the polarization resistance is prone to long term degradation effects probably due to Si segregation [44], cf. Fig. 8, thus being also rather impractical for comparing size effects. The chemical capacitance, however, is only weakly thermally activated [45] and, being a property of the GDC bulk [39], not affected by surface impurities. Furthermore, as stated above, the YSZ bulk resistance is not explicitly extracted with the equivalent circuit in Fig. 8.

In Fig. 9 the chemical capacitance of GDC microelectrodes of type A, B and C are plotted against the electrode surface area. As explained above since the GDC layer of all the electrodes is of the same thickness it should scale linearly with the electrode area, if the complete electrode area is probed by the current collector. This is indeed the case for all three electrode types. The volume specific chemical capacitance was calculated from the slope of the regression lines in Fig. 9. The values

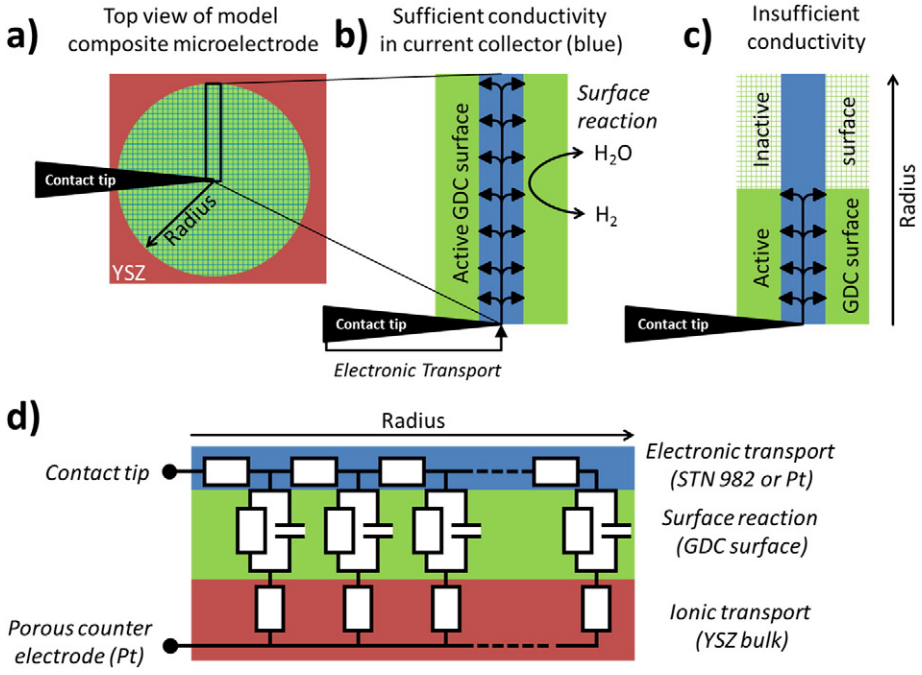

Fig. 7. Model of electronic and ionic charge transport in model composite microelectrodes. a) Top view of a contacted microelectrode with a grid shaped current collector; compare also Fig. 4d) for a side view; b) Magnification of radial current collector strip, orthogonal strips are not shown, the good electronic conductivity of the current collector allows the surface exchange reaction to happen along the whole diameter of the electrode; c) Insufficient electronic conductivity in the current collector phase limits the active surface in the radial direction of the microelectrode. d) Equivalent circuit describing the processes shown in b) and c): Electronic transport in the current collector phase (blue), surface oxygen exchange reaction on GDC (green) described by the polarization resistance parallel to the chemical capacitance of GDC [38–40] and oxygen ion transport in the YSZ substrate (red).

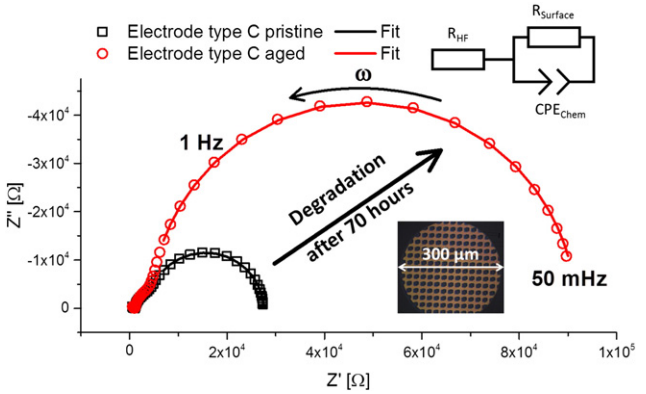

Fig. 8. Nyquist plots of electrochemical impedance spectra taken on 300 µm diameter electrode of type C, see Fig. 4b), with a 200 nm STN-982 current collector on 200 nm GDC-20 and an additional buried 100 nm thick Pt current collector. The current collector grids both were of 10 µm width and 10 µm spacing, see micrograph inset. The two spectra are taken 70 h apart on the same electrode, showcasing the degradation phenomena. The equivalent circuit to fit the data points is plotted in the inset in the top right, the fits to the data are shown as solid lines. Measurements were performed in a symmetrically heated setup and a gas atmosphere of humidified ~2.5 vol% H_2 in Ar, with a ratio of hydrogen to water of 1:1. The complete data of the polarization resistance degradation, also involving sulphur poisoning, is shown in Fig. 10c).

are given in Table 2 and agree reasonably for each electrode type. These results prove that at least in microelectrode experiments, STN-982 performs as efficient as platinum as a current collector.

3.3. Sulphur tolerance of microelectrodes with STN-982 current collectors

In Fig. 10 the long term evolutions of the surface polarization resistances of circular GDC composite microelectrodes of type A, B and C – cf. Fig. 4a), b) and c), respectively – during a sulphur poisoning experiment are plotted. All three electrodes exhibit comparable initial surface resistances, which have been corrected to account for the coverage of the STN-982 grid on layers B and C. Additionally, each electrode shows a linear degradation rate with time before the actual sulphur poisoning is started, cf. Fig. 6 and see Table 3 for the values. The initial degradation

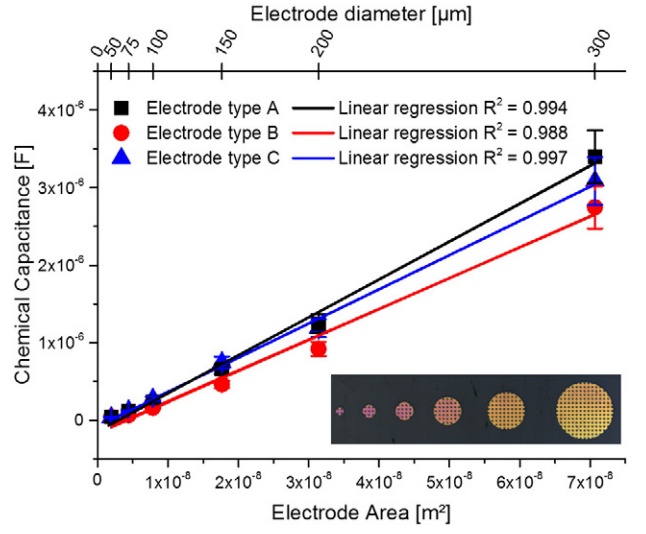

Fig. 9. Chemical capacitance of electrodes of type A, B and C, see Fig. 4, as a function of electrode area and linear regressions. Electrode diameter is plotted on the top X axis; the inset shows a micrograph of differently sized electrodes of type A as an example. All GDC layers were of 200 nm thickness, the oxidic current collectors of type B and C were 200 nm of STN-982. All current collector grids had a width and spacing of 10 µm. Relative errors of 10% are included in the plot, estimated from inaccuracies in layer thickness, electrode diameter and fits of the corresponding impedance spectra. Measurements were performed at 750 °C in an asymmetrically heated setup in a gas atmosphere of humidified ~2.5 vol% H_2 in Ar, with a ratio of hydrogen to water of 1:1.

Table 2
Volume specific chemical capacitances C_{chem}/m^3 calculated from the slope of the regression lines in Fig. 9, divided by the film thickness of 200 nm. Relative errors of 10% are estimated from inaccuracies in layer thickness, electrode diameter and fit accuracy.

	Volume specific C_{chem} [F/m^3]
Electrode type A	$2.5 \times 10^8 \pm 0.3 \times 10^8$
Electrode type B	$2.0 \times 10^8 \pm 0.2 \times 10^8$
Electrode type C	$2.2 \times 10^8 \pm 0.2 \times 10^8$

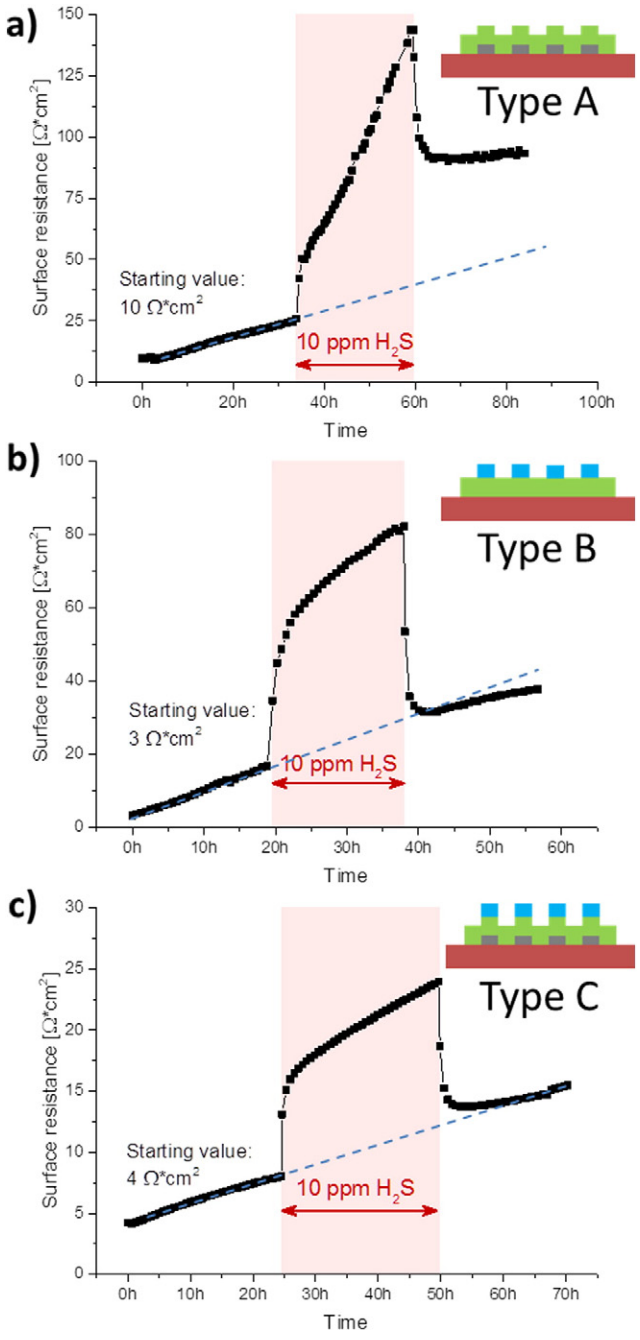

Fig. 10. Long term evolution of the surface polarization resistance during sulphur poisoning experiments of different electrode types, see Fig. 4, a) Type A, b) Type B and c) Type C, the GDC layers were of 200 nm thickness, the current collector of A is 100 nm Pt, the oxide current collectors of electrodes B and C were made of 200 nm of STN-982. Measurements were performed at 750 °C in a symmetrically heated setup in a gas atmosphere of humidified ~2.5 vol% H_2 in Ar, with a ratio of hydrogen to water of 1:1.

Table 3
Initial surface polarization resistances and degradation rates, before, during and after a sulphur poisoning phase corresponding to the data plotted in Fig. 10. Electrode types A, B, and C are described in Fig. 4, the oxidic current collector was STN-982 on electrodes B and C. The thickness of the GDC-20 layer was 200 nm, that of the Pt grid 100 nm on 5 nm Ti. Each electrode was 300 μm in diameter, the current collector grids were of 10 μm width with 10 × 10 μm holes. Measurements were performed at 750 °C in humidified ~2.5 vol% H2 in Ar, with a ratio of hydrogen to water of 1:1. The concentration of hydrogen sulphide during the poisoning phase was 10 ppm.

		Degradation rate		
	Initial resistance [Ω × cm^2]	Before sulphur poisoning [Ω × cm^2/h]	During sulphur poisoning [Ω × cm^2/h]	After sulphur poisoning [Ω × cm^2/h]
Electrode A	10	0.5	4.2	0.2
Electrode B	3	0.7	1.5	0.4
Electrode C	4	0.2	0.3	0.1

rates are extrapolated as dashed lines in Fig. 10. Results of one of our recent studies strongly suggested that this continuous decrease is caused by an accumulation of a siliceous phase on the surface of the GDC layer [44], which either originates from the quartz parts of the setup [46], the YSZ single crystal [47,48] or the GDC itself [10].

As soon as 10 ppm hydrogen sulphide is mixed into the gas atmosphere, a fast step-like increase is observed on all three samples followed by a regime of an increased predominantly linear degradation rate; the values are listed in Table 3. Upon closing the hydrogen sulphide gas supply, it is obvious that electrode A retains irreversible surface resistance degradation from the sulphur poisoning experiment, at least in the time monitored in this experiment. In a previous study on electrodes of type A, this behaviour was explained by H_2S adsorption and incorporation of sulphide ions into the GDC lattice [44], where the adsorption is reversible, but the GDC bulk changes takes longer to recover. This interpretation is in agreement with the results of a study on sulphur sorbents based on ceria, where a very similar time dependence for sulphur uptake and adsorption is found as in Fig. 10a) for the surface resistance [49]. Furthermore, another study on methane oxidation found two processes involved in the interaction of H_2S with ceria: A fast process ascribed to adsorption and a slower one associated with sulphur dissolution in the ceria bulk [50]. This sulphur scavenging effect was also used for explaining the enhanced sulphur resiliance of ceria or doped ceria modified porous Ni/YSZ SOFC anodes compared to unmodified ones [51]. In contrast, electrodes B and C quickly recover completely from the resistance increase during sulphur poisoning, as shown by the agreement of the resistance values after the poisoning phase with the extrapolated *Si*-associated degradation rate discussed before, see Fig. 10b) and c). In literature a promotional effect of hydrogen sulphide on methane conversion on a porous LST-46/YSZ anode has been reported [13]. It is postulated that the titanate dissociates hydrogen sulphide and becomes covered with a sulphur species [52,53], which exhibits catalytical activity. However, whether or not this mechanism is applicable in the present case cannot be judged unambiguously from the data available so far. Nevertheless, STN-982 seems to protect the GDC layer from irreversible degradation by sulphur poisoning. The elucidation of the exact mechanism will have to be a topic of a future study.

4. Conclusions

Conductivities of electronically conducting oxides, including La and Nb doped strontium titanates and alumina doped zinc oxide, were measured by the van der Pauw method. The best performing materials were incorporated as current collectors into model-composite microelectrodes based on GDC-20 and tested for stability in reducing atmospheres and the ability to transport charge to the whole electrode. Niobium doped strontium titanate (STN-982) showed comparable performance to platinum when used as a current collector, even though some conductivity degradation was encountered after repeated thermal cycling. In a sulphur poisoning experiment the GDC microelectrodes using STN-982 current collectors showed no sulphur related irreversible degradation effect, while the surface polarization resistance of a model composite electrode with only burried Pt current collectors retained some of the sulphur induced resistance increase. These results show that fully oxidic SOFC composite anodes of doped STO and GDC may offer significant advantages over the standard Ni/YSZ cermet regarding sulphur poisoning and, due to the absence of a metallic phase, improved redox cycling stability.

Acknowledgements

The financial support by the Austrian Federal Ministry of Science, Research and Economy and the National Foundation for Research, Technology and Development is gratefully acknowledged. Moreover, this study was financially supported by the Austrian Science Fund (FWF); Project F4509-N16 (SFB FOXSI). The authors thankfully acknowledge Elisabeth Eitenberger for recording the EDX spectra.

References

[1] N. Mahato, A. Banerjee, A. Gupta, S. Omar, K. Balani, Prog. Mater. Sci. 72 (2015) 141.
[2] A. Faes, A. Hessler-Wyser, A. Zryd, Membranes 2 (3) (2012) 585.
[3] J.L. Young, V. Vedharathinam, V.I. Birss, Solid Oxide Fuel Cells 12 (Sofc Xii) 35 (1) (2011) 1697.
[4] Z. Cheng, J.H. Wang, Y.M. Choi, L. Yang, M.C. Lin, M.L. Liu, Energy Environ. Sci. 4 (11) (2011) 4380.
[5] M.Y. Gong, X.B. Liu, J. Trembly, C. Johnson, J. Power Sources 168 (2) (2007) 289.
[6] L. Zhang, S.P. Jiang, H.Q. He, X. Chen, J. Ma, X.C. Song, Int. J. Hydrog. Energy 35 (22) (2010) 12359.
[7] X.L. Zhao, Q. Zhong, L. Gan, L.D. Li, Ionics 22 (8) (2016) 1415.
[8] S. Cho, D.E. Fowler, E.C. Miller, J.S. Cronin, K.R. Poeppelmeier, S.A. Barnett, Energy Environ. Sci. 6 (6) (2013) 1850.
[9] S.W. Tao, J.T.S. Irvine, Nat. Mater. 2 (5) (2003) 320.
[10] W.C. Chueh, Y. Hao, W. Jung, S.M. Haile, Nat. Mater. 11 (2) (2012) 155.
[11] W.C. Chueh, A.H. McDaniel, M.E. Grass, Y. Hao, N. Jabeen, Z. Liu, S.M. Haile, K.F. McCarty, H. Bluhm, F. El Gabaly, Chem. Mater. 24 (10) (2012) 1876.
[12] R. Mukundan, E.L. Brosha, F.H. Garzon, Electrochem. Solid-State. 7 (1) (2004) A5.
[13] A.L. Vincent, J.L. Luo, K.T. Chuang, A.R. Sanger, Appl. Catal. B Environ. 106 (1-2) (2011) 114.
[14] J. Nielsen, B.R. Sudireddy, A. Hagen, A.H. Persson, J. Electrochem. Soc. 163 (6) (2016) F574.
[15] L.J. van der Pauw, Philips Res. Rep. 13 (1958) 1.
[16] T.M. Huber, A.K. Opitz, M. Kubicek, H. Hutter, J. Fleig, Solid State Ionics 268 (2014) 82.
[17] A.V. Singh, R.M. Mehra, N. Buthrath, A. Wakahara, A. Yoshida, J. Appl. Phys. 90 (11) (2001) 5661.
[18] U. Ozgur, Y.I. Alivov, C. Liu, A. Teke, M.A. Reshchikov, S. Dogan, V. Avrutin, S.J. Cho, H. Morkoc, J. Appl. Phys. 98 (4) (2005) 041301.
[19] T.A. Adams, J. Nease, D. Tucker, P.I. Barton, Ind. Eng. Chem. Res. 52 (9) (2013) 3089.
[20] X.M. Ge, S.H. Chan, Q.L. Liu, Q. Sun, Adv. Energy Mater. 2 (10) (2012) 1156.
[21] T. Kolodiazhnyi, A. Petric, J. Electroceram. 15 (1) (2005) 5.
[22] X.L. Huang, H.L. Zhao, W.H. Qiu, W.J. Wu, X. Li, Energy Convers. Manag. 48 (5) (2007) 1678.
[23] O.A. Marina, N.L. Canfield, J.W. Stevenson, Solid State Ionics 149 (1-2) (2002) 21.
[24] R. Moos, K.H. Hardtl, J. Appl. Phys. 80 (1) (1996) 393.
[25] R. Meyer, A.F. Zurhelle, R.A. De Souza, R. Waser, F. Gunkel, Phys. Rev. B 94 (11) (2016) 115408.
[26] F. Gunkel, P. Brinks, S. Hoffmann-Eifert, R. Dittmann, M. Huijben, J.E. Kleibeuker, G. Koster, G. Rijnders, R. Waser, Appl. Phys. Lett. 100 (5) (2012) 052103.
[27] F. Gunkel, R. Waser, A.H.H. Ramadan, R.A. De Souza, S. Hoffmann-Eifert, R. Dittmann, Phys. Rev. B 93 (24) (2016) 245431.
[28] W. Menesklou, H.-J. Schreiner, K.H. Härdtl, E. Ivers-Tiffée, Sensors Actuators B Chem. 59 (2–3) (1999) 184.
[29] J.B. Goodenough, Annu. Rev. Mater. Res. 33 (2003) 91.
[30] C. Chen, D.J. Chen, W.C. Chueh, F. Ciucci, Phys. Chem. Chem. Phys. 16 (23) (2014) 11573.
[31] B.A. Boukamp, Solid State Ionics 169 (1-4) (2004) 65.
[32] B.A. Boukamp, J. Electrochem. Soc. 142 (6) (1995) 1885.
[33] A.T. Atimtay, S.L. Littlefield, Abstr. Pap. Am. Chem. Soc. 194 (1987) 121.

[34] E. Kazakevicius, G. Tsekouras, K.A. Michalow-Mauke, S. Kazlauskas, T. Graule, Fuel Cells 14 (6) (2014) 954.
[35] G.L. Xiao, S. Nuansaeng, L. Zhang, S. Suthirakun, A. Heyden, H.C. zur Loye, F.L. Chen, J. Mater. Chem. A 1 (35) (2013) 10546.
[36] M.D. Gross, K.M. Carver, M.A. Deighan, A. Schenkel, B.M. Smith, A.Z. Yee, J. Electrochem. Soc. 156 (4) (2009) B540.
[37] B.R. Sudireddy, P. Blennow, K.A. Nielsen, Solid State Ionics 216 (2012) 44.
[38] A. Nenning, A.K. Opitz, T.M. Huber, J. Fleig, Phys. Chem. 16 (40) (2014) 22321.
[39] W.C. Chueh, S.M. Haile, Phys. Chem. 11 (37) (2009) 8144.
[40] W. Lai, S.M. Haile, J. Am. Ceram. Soc. 88 (11) (2005) 2979.
[41] J. Fleig, F.S. Baumann, V. Brichzin, H.R. Kim, J. Jamnik, G. Cristiani, H.U. Habermeier, J. Maier, Fuel Cells 6 (3-4) (2006) 284.
[42] M. Gerstl, E. Navickas, G. Friedbacher, F. Kubel, M. Ahrens, J. Fleig, Solid State Ionics 185 (1) (2011) 32.
[43] W.C. Chueh, W. Lai, S.M. Haile, Solid State Ionics 179 (21-26) (2008) 1036.
[44] M. Gerstl, A. Nenning, R. Iskandar, V. Rojek-Woeckner, M. Bram, H. Hutter, A.K. Opitz, Materials 9 (8) (2016) 649.
[45] P. Velicsanyi, M. Gerstl, A. Nenning, H. Hutter, J. Fleig, A.K. Opitz, ECS Trans. 68 (2015) 1509.
[46] P. Singh, S.D. Vora, Advances in Solid Oxide Fuel Cells: Ceramic Engineering and Science Proceedings, John Wiley & Sons, Inc., 2008 99–110.
[47] M. de Ridder, R.G. van Welzenis, H.H. Brongersma, U. Kreissig, Solid State Ionics 158 (1-2) (2003) 67.
[48] M. de Ridder, A.G.J. Vervoort, R.G. van Welzenis, H.H. Brongersma, Solid State Ionics 156 (3) (2003) 255.
[49] M. Kobayashi, M. Flytzani-Stephanopoulos, Ind. Eng. Chem. Res. 41 (13) (2002) 3115.
[50] G. Postole, F. Bosselet, G. Bergeret, S. Prakash, P. Gelin, J. Catal. 316 (2014) 149.
[51] J.W. Yun, S.P. Yoon, S. Park, H.S. Kim, S.W. Nam, Int. J. Hydrog. Energy 36 (1) (2011) 787.
[52] D.D. Beck, J.M. White, C.T. Ratcliffe, J. Phys. Chem.-Us 90 (14) (1986) 3123.
[53] D.D. Beck, J.M. White, C.T. Ratcliffe, J. Phys. Chem.-Us 90 (14) (1986) 3132.